Published on 03 January 2023. Downloaded by CHANG GUNG UNIVERSITY on 2/9/2023 4:28:16 AM.

Nanoscale

ROYAL SOCIETY OF CHEMISTRY

PAPER

View Article Online
View Journal

Cite this: DOI: 10.1039/d2nr05847b

Dramatic improvement in the stability and mechanism of high-performance inverted polymer solar cells featuring a solution-processed buffer layer†

Yun-Ming Sung,[a,b] Cheng-Hsun-Tony Chang,[c] Cheng-Si Tsao,*[a] Hua-Kai Lin,[a] Hou-Chin Cha,[a] Pei-Cheng Jiang,[c] Tian-Cheng Liu,[a] Kang-Wei Chang,[d] Yu-Ching Huang*[d] and Jyh-Shen Tsay*[e]

Received 21st October 2022,
Accepted 1st January 2023

DOI: 10.1039/d2nr05847b

rsc.li/nanoscale

In this study, we demonstrate inverted PTB7:$PC_{71}BM$ polymer solar cells (PSCs) featuring a solution-processed s-MoO_3 hole transport layer (HTL) that can, after thermal aging at 85 °C, retain their initial power conversion efficiency (PCE) for at least 2200 h. The T_{80} lifetimes of the PSCs incorporating the novel s-MoO_3 HTL were up to ten times greater than those currently reported for PTB7- or low-band-gap polymer:PCBM PSCs, the result of the inhibition of burn-in losses and long-term degradation under various heat-equivalent testing conditions. We used X-ray photoelectron spectroscopy (XPS) to study devices containing thermally deposited t-MoO_3 and s-MoO_3 HTLs and obtain a mechanistic understanding of how the robust HTL is formed and how it prevented the PSCs from undergoing thermal degradation. Heat tests revealed that the mechanisms of thermal inter-diffusion and interaction of various elements within active layer/HTL/Ag electrodes controlled by the s-MoO_3 HTL were dramatically different from those controlled by the t-MoO_3 HTL. The new prevention mechanism revealed here can provide the conceptual strategy for designing the buffer layer in the future. The PCEs of PSCs featuring s-MoO_3 HTLs, measured in damp-heat (65 °C/65% RH; 85 °C per air) and light soaking tests, confirmed their excellent stability. Such solution-processed MoO_3 HTLs appear to have great potential as replacements for commonly used t-MoO_3 HTLs.

Introduction

Polymer solar cells (PSCs) are attractive emerging next-generation solar cells because of their low cost, low energy consumption, low carbon emission, light weight, flexibility, transparency, solution-printability, and ease of fabrication. Recently, the power conversion efficiencies (PCEs) of non-fullerene PSCs have progressed rapidly, now exceeding 18.2%[1] and achieving the requirements for commercialization. Nevertheless, the stability of high-performance PSCs has been a bottleneck affecting their commercialization. PSCs can be divided into conventional and inverted structures based on the positions of their hole transport layers (HTLs) and electron transport layers (ETLs). Unlike conventional PSCs that feature PEDOT:PSS or LiF as the HTL, inverted PSCs contain metal oxide layers as both the HTL and ETL and are usually more stable when based on the same active layer.[2–4] A commonly adopted model system for high-performance inverted PSCs involves blends of the low-band-gap (LBG) polymer poly[[4,8-bis[(2-ethylhexyl)oxy]benzo[1,2-*b*:4,5-*b*′]dithiophene-2,6-diyl][3-fluoro-2-[(2-ethylhexyl)carbonyl]thieno[3,4-*b*]thiophenediyl]] (PTB7) and [6,6]-phenyl-C_{71}-butyric acid methyl ester ($PC_{71}BM$). The PCEs of inverted PTB7-based PSCs operated without temperature- and light-stress conditions have low burn-in losses (≤10%) and values of T_{80}—the operating lifetime during which the PCE reaches 80% of its initial value—of greater than 35 days.[5]

The degradation mechanisms of PSCs can be divided into three categories:[6] (i) extrinsic degradation caused by chemical reactions with H_2O and O_2 from the atmosphere (minimized through encapsulation of the device), (ii) intrinsic degradation

[a]Institute of Nuclear Energy Research, Longtan, Taoyuan 32546, Taiwan. E-mail: cstsao@iner.gov.tw
[b]Institute of Atomic and Molecular Sciences, Academia Sinica, Taipei 10617, Taiwan
[c]Department of Electronic Engineering, Minghsin University of Science and Technology, Hsinchu 30401, Taiwan
[d]Department of Materials Engineering, Ming-Chi University of Technology, New Taipei City 24301, Taiwan. E-mail: huangyc@mail.mcut.edu.tw
[e]Department of Physics, National Taiwan Normal University, Taipei 116, Taiwan. E-mail: jstsay@phy.ntnu.edu.tw

† Electronic supplementary information (ESI) available. See DOI: https://doi.org/10.1039/d2nr05847b

Published on 03 January 2023. Downloaded by CHANG GUNG UNIVERSITY on 2/9/2023 4:28:16 AM.

caused by the elevated temperatures during operation in the dark, and (iii) intrinsic photoinduced degradation; the latter two will occur even in the case of perfect encapsulation. The temporal variations in the PCE degradation of PSCs are typically divided into three regimes: an initial period of rapid decay (the "burn-in" regime), a subsequent period of slow (or relatively stable) degradation that lasts for the solar cell's usable lifetime (the "long-term" regime), and a final period of rapid and complete degradation (the "failure" regime). If the burn-in degradation (usually 10–50%) is greater than 20%, the value of T_{80} can be very short and possibly even less than the burn-in time. If the burn-in loss is less than 20%, the value of T_{80} can be affected slightly by a very short burn-in period. Therefore, effectively minimizing the burn-in loss should enhance both the performance and the duration of stable operation, the critical factors affecting the commercialization of PSCs.

The burn-in degradation of a PSC is caused by several factors, including the polymer crystallinity,[7–9] fullerene oligomerization[10] and aggregation,[11,12] photoinduced defects,[13,14] and spinodal de-mixing.[15] The mechanisms of burn-in loss for PCEs operated at high temperature[6] are (i) macro-phase separation of the bulk heterojunction (BHJ) structure of the active layer[11,12] and (ii) the formation of a charge blocking layer at the interface between the Ag electrode and the charge transport layer.[16] The degradation in PCE caused by macro-phase separation can be suppressed through crosslinking or employing a polymer with a high glass transition temperature.[17] The most common approach for overcoming degradation at the HTL–electrode interface is the use of thermally evaporated MoO_3 as the HTL; it ensures good performance because of its low work function and favorable energy level diagram, relative to those of other metal oxides tested for inverted PSCs. Unfortunately, inverted PSCs incorporating thermally evaporated MoO_3 also display stability problems. It was reported recently[18] that an inverted PTB7:PC_{71}BM PSC that had been pre-aged at 85 °C for a long time (*i.e.*, aged prior to HTL/electrode deposition) exhibited a thermally stable BHJ morphology and little burn-in degradation; thus, the cell displayed good thermal stability. In contrast, the corresponding inverted PTB7:PC_{71}BM PSC that had been post-aged at 85 °C (*i.e.*, aged after HTL/electrode deposition) experienced high burn-in degradation within a short period of time, primarily as a result of inter-mixing of the interfacial layers of the cell. Chambon *et al.*[19] reported that the thermal diffusion of elements from the thermally evaporated MoO_3 HTL and Ag top electrode into the active layer was the main cause of the thermal burn-in loss in inverted PSCs. Hermerschmidt *et al.*[20] demonstrated that device degradation (thermal burn-in loss > 40%) was caused primarily by the interface between the evaporated MoO_3 HTL and the active layer and secondarily by the interface between the MoO_3 HTL and the Ag electrode. They employed interfacial/buffer engineering (*i.e.*, MoO_3/PEDOT:PSS/Ag electrode) to minimize the burn-in effect, but this approach also decreased the initial PCE. Greenbank *et al.*[21] proposed that the degradation was caused mainly by the interface between the MoO_3 HTL and the Ag electrode (leading to *ca.* 50% burn-in loss at 80 °C in a dark glove box, followed by a value of T_{s80} of *ca.* 500 h). Recently, Griffin *et al.*[22] and Ahmadpour *et al.*[23] demonstrated that thermally evaporated MoO_3 might undergo a change in the oxidation state of its Mo(VI) metal center when exposed to heat or light, leading to a change in work function and, thus, a degradation in PCE. Evaporated MoO_3 is also sensitive to included H_2O and O_2, which could change its work function and conductivity, thereby leading to a shorter lifetime.[24,25] Accordingly, the use of solution-processed MoO_3, or another metal oxide, as the HTL in the inverted PSC, instead of a thermally evaporated metal oxide, might possibly be an effective approach toward minimizing the burn-in loss, increasing the value of T_{80} and enhancing the possibility of PSC commercialization. Thermally evaporated WO_3 has displayed high thermal stability in inverted PSCs.[21] Although a few studies have demonstrated the use of solution-processed MoO_3 in the production of efficient inverted and conventional PSCs,[26–29] processing solution-processed MoO_3 HTLs remains challenging and there have been few investigations of their stability.

In this paper, we describe a solution-processed MoO_3 ("s-MoO_3") HTL that effectively minimizes thermal burn-in loss and, thus, enhances the stability of inverted high-performance LBG PSCs relative to that of their counterparts incorporating a thermally deposited MoO_3 ("t-MoO_3") HTL. For evaluation, we performed two accelerated lifetime tests: (i) accelerated heat tests based on the ISOS-D-2 protocol (in the dark and under N_2 at 65 and 85 °C, respectively) and (ii) accelerated damp-heat tests, including the ISOS-D-3 protocol (65 °C/65% RH and 85 °C/air).[30] At 85 °C under N_2, the inverted PTB7:PC_{71}BM PSC devices incorporating the s-MoO_3 HTL retained their PCE for more than 2000 h, with exceptional intrinsic stability in the burn-in and long-term regimes. This stability greatly exceeded the same-condition records currently reported for inverted LBG-based PSCs containing solution-processed PEDOT:PSS[20] and metal oxide[8,31] HTLs. In contrast, under the same conditions, the inverted PTB7:PC_{71}BM PSC featuring the t-MoO_3 HTL experienced a PCE burn-in loss of 20% within a few hours. Thus, novel s-MoO_3 HTLs can indeed be prepared for high-stability inverted PSCs. Moreover, we investigated the mechanism through which this solution-processed MoO_3 effectively inhibited the transfer of both Ag atoms (from the top electrode) and MoO_3 particles into the active layer, hoping to facilitate the future development of device architectures and processing methods for interface and buffer layer engineering of high-intrinsic-stability PSCs. We used X-ray photoelectron spectroscopy (XPS) to determine the elemental depth profiles through a systematic study of the thermal inter-diffusion and interactions of various elements within the various active layer/HTL/Ag electrode structures in response to various heat tests. We correlated the evolution of the elemental depth profiles in the device architectures with their stability under various heating conditions. Based on the XPS data, we propose the following sequential steps for the formation of such robust HTL layers and their interfaces: (i) diffusion of s-MoO_3 and

 This journal is © The Royal Society of Chemistry 2023

Published on 03 January 2023. Downloaded by CHANG GUNG UNIVERSITY on 2/9/2023 4:28:16 AM.

solvent molecules into the active layer during HTL coating, (ii) thermal diffusion of s-MoO_3 from the active layer toward the HTL ("backward diffusion"), and (iii) effective stabilization of the newly formed s-MoO_3 film structure and its interfaces to fully inhibit the penetration of Ag and MoO_3 into the active layer upon heating. The robust HTL and its associated contact interfaces also displayed effective resistance against invasive O_2 and H_2O, thereby enhancing the extrinsic stability, as evidenced in damp heat tests. Moreover, the results of light soaking tests confirmed that the good stability is because of the resistance to invasive O_2 and H_2O. Furthermore, the solution-processed MoO_3 HTL presented herein has several other attractive features such as the use of an environmentally friendly solvent, low cost, and a low-energy fabrication process.

Experimental

Materials preparation

ZnO nanoparticles. The preparation of the ZnO nanoparticle solution has been described previously by Wang *et al.*[32] Zinc acetate dehydrate (Alfa, 2.2 g) was dissolved in ethanol (Fisher, 100 mL) at room temperature. Lithium hydroxide monohydrate (Alfa, 0.58 g) was added to this solution and dispersed in an ultrasonic bath for 30 min. The color of the solution changed from gray to transparent during the dispersion process. Deionized water (2 mL) was added to the transparent solution and then the mixture was stirred in a water bath (60 °C) for 30 min. When the color of the stirred solution changes from transparent to white, the mixture was cooled to room temperature and centrifuged (3000 rpm, 3 min). After the suspension had been removed, the precipitates were re-dispersed in ethanol. By repeating this centrifugation process, the remaining ZnO precipitates were dispersed in isopropanol (IPA) at a concentration of 10 mg mL^{-1}, with 0.15% ethanolamine as a dispersant, and then filtered through a 0.45-μm PVDF filter. The average size of the resulting ZnO nanoparticles was 7 nm.

s-MoO_3 solution. The materials for the preparation of the solution for the s-MoO_3 HTL included molybdenum powder (≤4 μm, Strem), ethanol, and 30 wt% hydrogen peroxide (ACROS). Molybdenum powder (0.1 g) was dispersed in ethanol (10 mL) in an ultrasonication bath for 30 min and then hydrogen peroxide (30 wt%, 0.35 mL) was added into the solution. The blended solution was then stirred at room temperature for 20 h, at which point the color of the solution changed from black to blue—an indicator of the hydrogen transition metal (HTM) bronze.[33] The blue solution was filtered through a 0.45-μm PVDF filter and then dried under vacuum. The dried powder was dissolved in ethanol (10 mL) by stirring at room temperature for 1 day, thereby completing the preparation of the solution for the s-MoO_3 HTL. A solution-processed MoO_3 HTL[34] has previously been reported in the preparation of a conventional type of PSC structure. In this present study, IPA was added into the s-MoO_3 solution at an s-MoO_3-to-IPA ratio of 1 : 3 to ensure a good coating of a uniform film on the active layer.

Active layer solution. The active layer solution was prepared by blending PTB7 (1-material, 10 mg) and $PC_{71}BM$ (Nano-C, 15 mg) in *o*-xylene (Sigma-Aldrich, 1 mL) containing 1,8-diiodooctane (DIO, Sigma-Aldrich, 3%) as an additive. The other active layer solution was prepared by blending PM6 (1-material, 8 mg) and Y6 (1-material, 9.6 mg) in chloroform (Sigma-Aldrich, 1 mL) containing 1-chloronaphthalene (CN, Sigma-Aldrich, 0.5 vol%) as an additive. The blended solution was stirred at 70 °C in a glove box for 1 day.

Device fabrication. The substrate, 5-Ω indium tin oxide (ITO) glass, was patterned by laser ablation. The ITO glass was washed with acetone, dried under a flow of N_2 gas, and cleaned in a plasma cleaner for 10 min. For coating the ETL, a solution of ZnO nanoparticles (10 mg mL^{-1}) was spin-coated onto the cleaned ITO glass up to a thickness of 30 nm. A PTB7:$PC_{71}BM$ solution was then coated on the ZnO ETL at 2000 rpm to achieve a layer thickness of 80 nm, followed by drying under vacuum for 1 day to remove any residual solvents. A PM6:Y6 solution was coated on the ZnO ETL at 5000 rpm to achieve a layer thickness of 100 nm, followed by annealing at 110 °C for 10 min. The t-MoO_3 HTL (thickness: 8 nm) was thermally evaporated onto the active layer at a deposition rate of 0.1 Å s^{-1} under 5.5×10^{-6} torr. To deposit the s-MoO_3 HTL, the s-MoO_3 solution was spin-coated onto the active layer at 3000 rpm for 30 s. The thickness of the optimized HTL was 14 nm. The active layer, ETL layer, and s-MoO_3 HTL were all deposited at room temperature and exposed to air. After the deposition of the s-MoO_3 HTL, Ag (100 nm) was thermally evaporated onto the HTL under 5.5×10^{-6} torr as the metal electrode. The device area of 1×0.3 cm^2 was defined by a mask. All of the PSCs for the lifetime tests had the inverted structure ITO/ZnO/PTB7:$PC_{71}BM$ or PM6:Y6/t-MoO_3 or s-MoO_3/Ag electrode. Prior to the damp heat and light soaking tests, the devices were encapsulated with UV epoxy (eGloo, SAES) under N_2 in a glove box.

Device characterization and methods, crystallography

Depth profiling measurement by XPS. Specimens grown on ITO glass were transferred to an ultrahigh vacuum chamber (base pressure: 6.7×10^{-10} mbar) for XPS analysis. A ULVAC-PHI 5000 Versa Probe photoelectron spectrometer, equipped with a monochromatic focused Al anode X-ray source and a 16-channel hemisphere analyzer (HSA), was employed for the XPS measurements. The power of the focused X-ray source was 30.9 W; the scan area was 100 × 100 $μm^2$. The take-off angle and pass energy of the HSA analyzer were 45° and 58.70 eV, respectively. A flooding electron gun and low-energy ion gun were employed for charge neutralization. Preliminary checks of three points randomly chosen on each specimen revealed that the compositional distribution was uniform.

Performance measurement and damp-heat tests. The voltage–current density curves of all of the PSC devices were measured under AM1.5G light (100 mW cm^{-2}) from a solar simulator (Model 11000, Abet Technologies). A profiler (Alpha Step D-100, KLA Tencor) was used to measure the real layer

Published on 03 January 2023. Downloaded by CHANG GUNG UNIVERSITY on 2/9/2023 4:28:16 AM.

thickness. To study the intrinsic degradation at high temperatures, the PSC devices were aged at 65 and 85 °C in the dark under N_2 in a glove box. The damp-heat tests of the encapsulated PSC devices were conducted under conditions of 65 °C/65% RH in an environmental chamber equipped with an automatic monitor and a constant temperature/humidity control (YEOW LONG Technology Developing Co.). These test conditions followed the ISOS-D-3 and SEMI PV76 (SEMI, 2016)[35] test standards, respectively. In addition, an encapsulated device was tested by placing it in an oven at 85 °C in ambient air (*ca.* 45% RH).

Impedance measurement. The impedance measurements were conducted by using an impedance spectrum analyzer (Zahner IM6) under air and in the dark conditions. The impedance results were measured by applying a DC voltage and an AC voltage of 0 V and 20 mV in the frequency range of 1 Hz to 3 MHz, respectively.

Light-soaking test. The light-soaking tests were conducted under ambient conditions with a UV filter (cut-off: 400 nm) under continuous AM 1.5G solar illumination (100 mW cm^{-2}) monitored by a photodetector (Model: KD-LS01-0808, King Design Industrial). The illumination area was 40 cm × 40 cm.

Results and discussion

Intrinsic thermal degradation under N_2 at 65 and 85 °C

For systematic comparison, we investigated the temperature dependence of the thermal burn-in loss and long-term degradation induced by the t-MoO_3 and s-MoO_3 HTLs under prolonged periods of thermal annealing. First, we considered only the intrinsic degradation effect. Fig. 1 and Fig. S1† display the degradations in PCEs of inverted PTB7:$PC_{71}BM$ devices incorporating the t-MoO_3 and s-MoO_3 HTL/Ag electrodes under thermal aging at 85 and 65 °C, respectively, in the dark under N_2 in a glove box. The data for the photovoltaic performance of the PSC devices based on the s-MoO_3 and t-MoO_3 HTL/Ag electrodes, aged at 85 °C, have been averaged from 14 and 5 devices, respectively. In Fig. 1, the initial PCE of the s-MoO_3-based devices was 6.35 ± 0.36%, with an open-circuit voltage (V_{oc}), short-circuit current density (J_{sc}), and a fill factor (FF) of 0.69 ± 0.03 V, 16.35 ± 0.58 mA cm^{-2}, and 56.69 ± 2.79%, respectively. The initial PCE of the t-MoO_3-based devices was 6.38 ± 0.39%, with the values of V_{oc} and J_{sc} and FF being 0.78 ± 0.00 V, 13.17 ± 0.40 mA cm^{-2}, and 61.93 ± 3.84%, respectively. Typical J–V curves for the PTB7:$PC_{71}BM$ devices with t-MoO_3 and s-MoO_3 HTL, respectively, are shown in Fig. S2 (ESI).† The PCEs of the devices incorporating t-MoO_3 HTLs (as the reference group) and aged at 85 and 65 °C decreased rapidly to 80 and 70%, respectively, of the initial efficiency (burn-in regime). The subsequent long-term stability regimes for the samples aged at 85 and 65 °C involved gradual decays to 60% of the initial efficiency lasting for 800 and 1200 h, respectively. The different aging temperatures affected the level of burn-in loss, as well as long-term stability, because of the different thermal diffusion kinetics of the charge traps in the active layers. In contrast, the normalized performance of the devices incorporating the s-MoO_3 HTL and aged at 85 °C in the dark under N_2 initially increased slightly and then became stable (or even increased slightly again thereafter) over a period of more than 2200 h, with neither burn-in loss nor long-term degradation. This intrinsic thermal stability was remarkable and exceptional, greatly exceeding the current data records reported for LBG PSC devices under similar thermal stresses or ambient conditions. The value of T_{80} of our device was up to ten times higher than those of PTB7:$PC_{71}BM$-based PSCs reported previously under various thermal-stress-equivalent tests.[8,32,36,37]

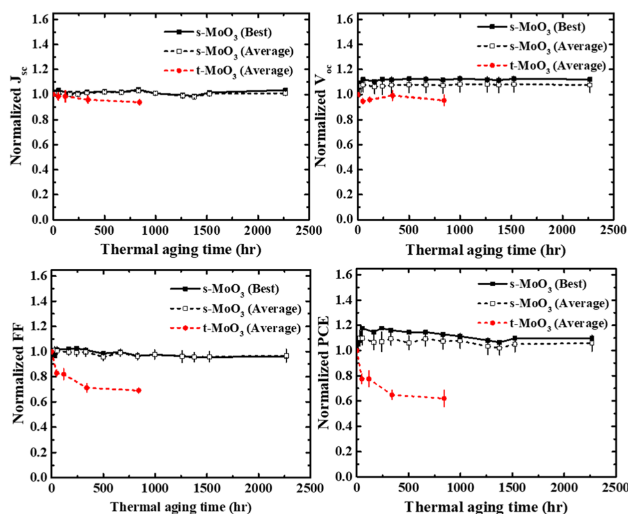

Fig. 1 Variations in the photovoltaic characteristics with respect to the thermal aging time of inverted PTB7:$PC_{71}BM$ devices incorporating t-MoO_3 and s-MoO_3 HTLs. All of the devices have been thermally aged at 85 °C in the dark under N_2 in a glove box. The solid curve represents the champion device and the dashed curves with error bars represent the averaged data.

Two mechanisms have been suggested previously to explain the thermal degradation behavior of inverted PSC incorporating t-MoO_3 HTLs. The first degradation mechanism involves the burn-in loss being caused partly by the rapid drop in the value of V_{oc}, as displayed in Fig. 1. In a previous study, we proposed that the thermal burn-in loss of the PCE was caused by the thermally evaporated MoO_3 particles diffusing far into the active layer to form charge traps (or defects) during the heating stress test.[18] Other studies have found that the initial decrease in the values of V_{oc} and the burn-in loss was caused by the diffused metals Mo and Ag acting as charge traps within the active layer.[19,38] The second degradation mechanism is closely related to the long-term stability, caused by the slight decline in the value of J_{sc} and the exponential decay of the FF. This degradation mechanism can be attributed to (i) a morphological change in the BHJ structure, (ii) a change in the work function of the interface of the MoO_3 HTL/Ag electrode,[22,39,40] (iii) a change in the oxidation state of Mo (VI),[22,23] (iv) an external agent (*e.g.*, O_2 or H_2O),[22,41,42] and (v) the diffused metals Mo and Ag acting as charge traps within the active layer.[19,38] In the previous studies,[17,18] the thermal

This journal is © The Royal Society of Chemistry 2023

Published on 03 January 2023. Downloaded by CHANG GUNG UNIVERSITY on 2/9/2023 4:28:16 AM.

degradation purely caused by the morphological change and vertical phase separation of the BHJ structure in the PTB7:$PC_{71}BM$-based active layer can be determined by heating the PSC devices without the HTL/Ag electrode at high temperatures for different times followed by the deposition of the HTL/Ag electrode and then PCE measurement. The degradation caused by the change in the BHJ structure of the PTB7:$PC_{71}BM$ active layer demonstrates a gradual decrease in 10% of the initial PCE under aging at 85 °C for 500 h.[18] We used atomic force microscopy to observe the topography of the PTB7:$PC_{71}BM$ active layers/8 nm t-MoO_3 and 15 nm s-MoO_3 with and without thermal aging at 85 °C for 100 h as shown in Fig. 2. The nanoscale domains of topography consist of the $PC_{71}BM$ aggregation clusters and PTB7 nanocrystals in the BHJ structure. The $PC_{71}BM$ clusters in the active layer with thermal aging are larger than those in the active layer without thermal aging, showing the thermally-phase-separated BHJ structure. The morphologies of PTB7:$PC_{71}BM$/8 nm t-MoO_3 and 15 nm s-MoO_3 are similar to each other before or after thermal aging. The RMS of PTB7:$PC_{71}BM$/8 nm t-MoO_3 is slightly reduced after thermal aging. The RMS of PTB7:$PC_{71}BM$/15 nm s-MoO_3 does not change after thermal aging. The topographies of ITO/8 nm t-MoO_3 (a) without and (b) with aging and ITO/15 nm s-MoO_3 (c) without and (d) with aging are shown in Fig. S3.† The morphology and RMS of ITO/8 nm t-MoO_3 are slightly smaller than those of ITO/15 nm s-MoO_3 because of the solution process. The RMS value almost does not change after thermal aging for both HTLs. In contrast, the PCE of the t-MoO_3-based device (the reference group) shows a burn-in loss of 20% in a short time and then a gradual decay to 60% of the initial efficiency lasting 800 h (Fig. 1d). Based on these two variations in PCE with respect to aging time, the degradation contribution purely caused by the BHJ structure of the active layer can be separated and thus the main (*i.e.*, the rest) contribution of the thermal degradation behavior can be roughly attributed to the thermal inter-diffusion and interaction of interfaces between the active layer/HTL/Ag electrode. The interfacial engineering[19–21,38] on the HTL/Ag electrode for the improvement of thermal stability becomes increasingly important except for the morphological and vertically compositional control of the active layer. The other factors, such as the chemical state, are regarded as minor factors and are not discussed here.

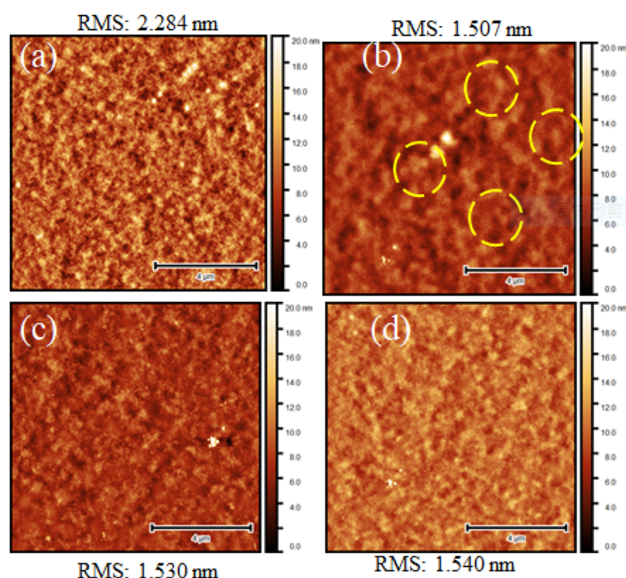

Fig. 2 Topographies of ITO/ZnO/PTB7:$PC_{71}BM$/8 nm t-MoO_3 (a) without and (b) with aging and ITO/ZnO/PTB7:$PC_{71}BM$/15 nm s-MoO_3 (c) without and (d) with aging. The thermal aging was performed at 85 °C for 100 h. The large $PC_{71}BM$ aggregation clusters or PTB7 crystalline domains in the phase-separated BHJ structure formed by thermal aging are marked by yellow circles. The scale bar is 4 μm. The RMS of ITO/ZnO/PTB7:$PC_{71}BM$ is 1.45 nm.

It seems that the s-MoO_3-based device can fully inhibit the degradation effect caused by the thermal inter-diffusion and interaction of interfaces between the active layer/HTL/Ag electrode. The initial increase in PCE is caused by the effective reinforcement of s-MoO_3 HTL and interface favorable charge transport (discussed later). The robust interface characteristics and the internal HTL structure may cause a slight increase or constant PCE with aging for long-term stability. In addition, the s-MoO_3-based device shows an increase in performance to compensate for the PCE loss caused by the increasing change in the BHJ structure of the active layer with aging time, keeping the initial PCE over a lasting period of 2200 h (the second degradation stage). It can be reasonably speculated that this PCE promotion is caused by the (1) improvement of interfacial contact (layer roughness) between the active layer and s-MoO_3 HTL and (2) the sintering of s-MoO_3 HTL due to thermal aging. The thermally-stable BHJ structure processed with DIO is also a factor of long-term stability. The alcohol treatment can decrease the domain size on and in the PTB7:$PC_{71}BM$ film and then improve the PCE and Jsc values. However, the average domain size is between 30 nm to 300 nm according to the literature,[43] whose scale is much larger than the size of the diffusion-in t-MoO_3 and s-MoO_3 species. Hence, it can be speculated that the alcohol treatment would not affect the thermal stability in this case.

PM6:Y6 PSC is a well-known non-fullerene-acceptor-based system with high performance. Recently, the thermal stability behavior at ≥80 °C of PM6:Y6 PSC has attracted more interest.[44–46] It is interesting to understand if the s-MoO_3 method is applicable to the PM6:Y6 PSC. We prepared the PSCs with PM6:Y6 as the active layer using chloroform solvent in a nitrogen glove box. Their inverted structures are ITO/ZnO/PM6:Y6/t-MoO_3 or s-MoO_3/Ag electrodes. The PCE values of t-MoO_3- and s-MoO_3-based PM6:Y6 PSCs are 14.33% and 12.28%, respectively, suggesting the applicability of s-MoO_3 HTL to this PM6:Y6 system. The corresponding current density–voltage curves and performance characteristics are shown in Fig. S4 and Table S1 (ESI).† Fig. 3 shows the representative behavior of thermal stability at 85 °C of t-MoO_3- and s-MoO_3-based PM6:Y6 PSCs. The normalized PCE of the device incorporating a t-MoO_3 HTL shows an exponential decay to 80% of the initial PCE (like burn-in loss) and remains stable

Published on 03 January 2023. Downloaded by CHANG GUNG UNIVERSITY on 2/9/2023 4:28:16 AM.

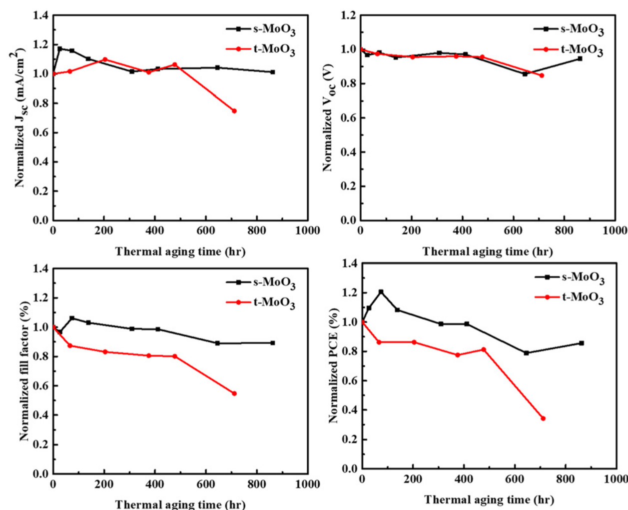

Fig. 3 Variation in the photovoltaic characteristics with respect to the thermal aging time of inverted PM6:Y6 devices incorporating t-MoO_3 and s-MoO_3 HTLs, respectively.

up to 480 h followed by failure. The thermal stability behavior at 85 °C of PM6:Y6 PSC reported by Chen *et al.*[44] also showed a similar decay of PCE to 80% of the initial value approaching 100 h. The main degradation reported may be due to the large aggregation of Y6 molecules in the BHJ structure of the active layer due to thermal aging. Han *et al.*[46] showed that the processed-ZnO electron transport layer for the aged PM6:Y6 PSC at 80 °C can reduce the burn-in loss. For the device incorporating s-MoO_3 HTL, the normalized PCE shows an initial increase lasting 100 h and then an exponential decay to 80% of the initial PCE lasting 860 h followed by a drastic drop. Both decay trends (long term stability) are similar and can be mainly attributed to the morphological evolution of the BHJ structure of the active layer. The effect of thermal diffusion between active layer/MoO_3/Ag layers on long-term degradation may be a minor factor in this case. Remarkably, the initial increase in PCE for the s-MoO_3-based PM6:Y6 PSC can be attributed to the effective reinforcement of the s-MoO_3 layer and interface between the active layer and HTL mentioned in the PTB7:$PC_{71}BM$ PSC case. The intrinsic thermal stability of the devices prepared with the novel s-MoO_3 HTL was not affected by either of the two degradation mechanisms discussed above. Therefore, we performed the following mechanistic study to determine how the presence and novel structure of the s-MoO_3 HTL fully inhibited the thermal degradation, potentially providing new insights for the future fabrication of the highly stable PSCs. Notably, the actual performance is shown in Fig. 3 and a representative behavior of decay curves is shown in Fig. S5†. Their initial PCEs are 7.5%–8%. The behavior of most of the data is similar to that of these data. In addition, the information of normalized and un-normalized decay curves of the t-MoO_3- and s-MoO_3-based PM6:Y6 PSCs (with PCE values similar to the devices mentioned in the manuscript, shown in Table S2†) are added to the ESI for better comparison (Fig. S6†). The difference between the decay curves of such two groups with different initial performances might be due to the BHJ structural damage by the thermal aggregation of the Y6 molecules mentioned. The BHJ structure with high performance is not favorable to stability. The present study is focused on the effect of HTL based on the relatively thermally stable BHJ structure such as PTB7:$PC_{71}BM$ PSC. PM6:Y6 PSC has a minor issue because its stability is subject to more other complex factors.

Y. Wang *et al.*[47] developed the hybrid MoO_3–PEDOT: PSS HTL. The MoO_3-induced oxidation doping in PEDOT: PSS can effectively suppress the interfacial chemical reactions between BHJ and PEDOT: PSS. This method retains the stable and high built-in potential across BHJ, which improves the operational stability of non-fullerene-based PSCs. W. Lan[48] incorporated CdSe@ZnS quantum dots (QD) to modify PEDOT: PSS HTL in which the coulombic attraction between the PEDOT units and PSS units is disturbed. The use of CdSe@ZnS QDs-PEDOT: PSS HEL decreases the reduction in PCE under accelerated UV aging test conditions. This modified HTL favors the efficient operation of the non-fullerene-based PSCs by maintaining a high built-in potential across BHJ and demonstrates the importance of interfacial engineering. W. Lan *et al.*[49] also prepared the PM6:non-fullerene acceptor PSC with a bilayer MoO_3/antimonene HEL which significantly improves the operational stability by maintaining a high built-in potential.

Degradation mechanism studied by XPS depth profiling and impedance spectroscopy

We used XPS to investigate the elemental depth profiles within the active layer/HTL/Ag electrode structures that have been subjected to different thermal aging tests to reveal both the degradation mechanism operating in the presence of the t-MoO_3 HTL and the so-called "protection" mechanism operating in the presence of the s-MoO_3 HTL. We simultaneously investigated both the thermal interlayer diffusion behavior and the interactions among the elements with respect to the vertical positions across the interfaces. To begin our systematic study, we considered only the effect of pure HTL on the active layer. We recorded the XPS spectra of Si substrate/ZnO/PTB7:$PC_{71}BM$/t-MoO_3 (t-MoO_3 thickness: 8 nm; as the top surface for XPS depth profiling) and Si substrate/ZnO/PTB7:$PC_{71}BM$/s-MoO_3 (s-MoO_3 thickness: 15 nm; as the top surface) structures before and after thermal aging at 85 °C for 70 h. Fig. 4a shows the intensity of the Mo and O signals with respect to the vertical depth from the surface of the HTL as a function of the sputtering time for the multilayer samples incorporating the t-MoO_3 HTL. Prior to thermal aging, the depth distributions of Mo and O were sharp Gaussian peaks that rapidly decreased to zero at the interface between the HTL and the active layer (after a sputtering time of *ca.* 2 min). After aging, the Mo and O distributions had broadened and the peaks had shifted to the interface, signifying that thermal diffusion of Mo and O atoms had occurred into the active layer. The Mo and O distributions ended after a sputtering time of 4 min. The depth profiles and thermal diffusion of the Mo and O atoms into the

 This journal is © The Royal Society of Chemistry 2023

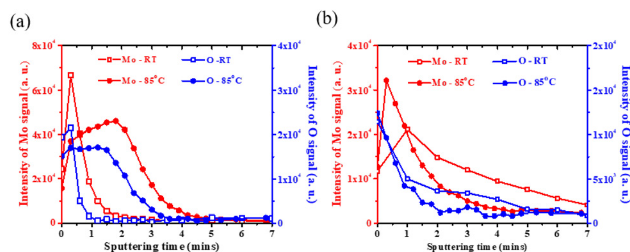

Fig. 4 XPS elemental depth profiles of Mo (3d) and O (1s) for (a) Si/ZnO/PTB7:$PC_{71}BM$/8 nm t-MoO_3 (as the top surface for sputtering) and (b) Si/ZnO/PTB7:$PC_{71}BM$/15 nm s-MoO_3 (as the top surface for sputtering) structures, measured before and after thermal aging at 85 °C for 70 h.

active layer were consistent with those determined previously using Auger electron spectroscopy (AES).[38] We have previously reported a degradation mechanism in which thermally diffused Mo atoms in the active layer can serve as recombination traps.[18]

Fig. 4b displays the intensity of the Mo and O signals with respect to the depth from the surface of HTL for multilayer samples featuring the s-MoO_3 HTL. Prior to thermal aging, the depth profiles of Mo and O distributions were remarkable, displaying slow exponential decay starting from the surface of the HTL. The Mo and O distributions extended into the deep interior of the active layer until the sputtering time reached 7 min. The sputtering rate of the polymer active layer is much faster than that of metal oxide HTL. We speculate that the s-MoO_3 particles had been deeply transferred into the active layer during the deposition of the HTL solution on the active layer, presumably because the s-MoO_3 particles could diffuse into the active layer along with the ethanol due to the low surface tension of solvent. Because these s-MoO_3 particles in the active layer could not serve as charge traps, the PSC devices exhibited good initial PCEs. The very low mismatch between the energy level of s-MoO_3 (−5.1 eV)[34] and the highest occupied molecular orbital (HOMO) of PTB7 (−5.15 eV)[50] allowed favorable hole hopping at the interfaces of PTB7/s-MoO_3/PTB7. Interestingly, the s-MoO_3 samples after thermal aging exhibited a rapid decay in the curves of the Mo and O distributions in the active layer, increasing toward the HTL, signifying the diffusion of all of the s-MoO_3 particles within the active layer back to the HTL and then forming a sharp interface (discrete in concentration) between the HTL and the active layer after a sputtering time of approximately 3 min. Eventually, almost no s-MoO_3 particles were present in the active layer. It seems that thermal aging at 85 °C had an inverse effect, enabling the s-MoO_3 HTL to have a well-defined interior structure, a sharp contact interface, and an enhanced chemical composition or oxidation state for MoO_x, resulting in the initial increase in PCE, instead of a burn-in loss, and excellent long-term stability. Moreover, this strengthening of the intrinsic stability by aging at 85 °C was not temporary, being unaffected by prolonged operation for over 2000 h. To the best of our knowledge, this extremely high thermal stability and novel layer structure, tuned by solution processing and inverse diffusion of s-MoO_3 particles, has not been reported previously as a processing strategy for PSCs with high thermal stability.

After demonstrating how the pure HTL interacted with the active layer under thermal conditions, we studied the influence of the incorporation of the Ag top electrode in these multilayer samples. We performed XPS with Si substrate/ZnO/PTB7:$PC_{71}BM$/t-MoO_3 (8 nm)/Ag (as the top surface for XPS depth profiling) and Si substrate/ZnO/PTB7:$PC_{71}BM$/s-MoO_3 (15 nm)/Ag (as the top surface for XPS depth profiling) structures after thermal aging at 85 °C for 70 h. The elemental depth profiles of Mo and O in the aged multilayer Si substrate/ZnO/PTB7:$PC_{71}BM$/t-MoO_3/Ag sample (Fig. 5a) revealed the inter-layer diffusion of t-MoO_3 particles into the Ag electrode from the interface between the HTL and the Ag layer (at a sputtering time of *ca.* 3 min). The t-MoO_3 HTL evolved into a MoO_3–Ag alloy and lost its hole-extraction properties. In addition, we observed the concomitant diffusion of Ag into the active layer through the whole t-MoO_3 HTL. This phenomenon has also been reported in other XPS and AES studies.[21,38] Significant amounts of Ag, Mo, and O atoms migrated across the interface between the t-MoO_3 HTL and the active layer (at a sputtering time of *ca.* 5 min), thereby acting as recombination centres or charge traps. Notably, the Ag, Mo, and O atoms reached a depth of 10 min of sputtering, much deeper in the active layer than they were in the pure t-MoO_3 HTL. The thermal migration of Ag atoms toward the active layer appeared to concurrently enhance the thermal diffusion and deep penetration of the Mo and O atoms into the active layer. The interlayer diffusion at the interfaces might also have caused unfavorable changes in the work function and could be correlated to the mechanism of degradation of the photovoltaic parameters, and could occur around the Ag–t-MoO_3 HTL and the t-MoO_3 HTL–active layer interface and in the t-MoO_3 HTL itself.

In contrast, the elemental depth profiles of the aged multilayer Si substrate/ZnO/PTB7:$PC_{71}BM$/s-MoO_3/Ag sample (Fig. 5b) revealed the sharp Gaussian peak distributions of the Mo and O atoms, which appeared to be totally confined within the s-MoO_3 HTL. Moreover, Ag atoms did not penetrate s-MoO_3 HTL and were blocked before the Ag–s-MoO_3 HTL interface at a sputtering time of approximately 3 min.

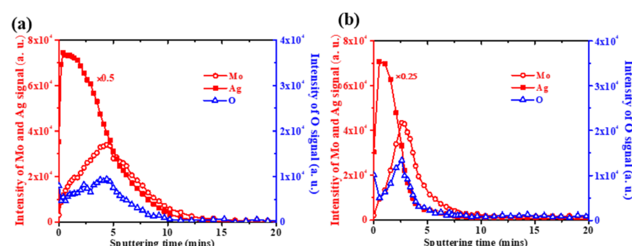

Fig. 5 XPS elemental depth profiles of Ag (3d), Mo (3d), and O (1s) for (a) Si/ZnO/PTB7:$PC_{71}BM$/8 nm t-MoO_3/15 nm Ag (as the top surface for sputtering) and (b) Si/ZnO/PTB7:$PC_{71}BM$/15 nm s-MoO_3/15 nm Ag (as the top surface for sputtering) structures, measured after thermal aging at 85 °C for 70 h.

Published on 03 January 2023. Downloaded by CHANG GUNG UNIVERSITY on 2/9/2023 4:28:16 AM.

Published on 03 January 2023. Downloaded by CHANG GUNG UNIVERSITY on 2/9/2023 4:28:16 AM.

Remarkably, the s-MoO_3 HTL had a robust structure and clear interface (between the s-MoO_3 layer and the active layer; at a sputtering time of *ca.* 6 min) that was formed or enhanced by the thermal backward diffusion of the s-MoO_3 particles from the active layer, thereby effectively inhibiting the thermal penetration or interlayer diffusion of Ag atoms. In other words, the s-MoO_3 HTL was not transformed into a MoO_3-Ag alloy and retained its good hole-extraction properties. The degradation factors closely related to the t-MoO_3 HTL were not in effect here, due to the presence of the s-MoO_3 HTL. Thus, the novel s-MoO_3 HTL structure fully inhibited the various thermal degradation processes or mechanisms caused by conventional metal oxide HTLs, as revealed through XPS depth profiling for the first time. We suggest the following mechanism for the formation of such a robust structure for the s-MoO_3 HTL and its interfaces: (i) s-MoO_3 diffused into the active layer with the help of the diffusing solvent molecules during the coating process of the s-MoO_3 HTL; (ii) the s-MoO_3 particles diffused back from the active layer to the s-MoO_3 HTL ("backward diffusion") upon heating; and (iii) the effective reinforcement of the s-MoO_3 film structure and interfaces against degradation occurred during the subsequent process of continuous heating. We speculate that the backward-diffusion of the s-MoO_3 particles is due to the evaporation and removal of the ethanol solvent during thermal aging. The s-MoO_3 particles are together with ethanol. The direction of the initial diffusion of ethanol is affected by the diffusion-in path. The backward diffusion of the s-MoO_3 particles toward the s-MoO_3 HTL effectively and simultaneously stopped the interlayer diffusion of Ag into the s-MoO_3 HTL and the active layer and the thermal diffusion of Mo into the active layer. Fig. 6 provides a schematic representation of the related thermal diffusion behaviors caused by t-MoO_3 and s-MoO_3, respectively.

In order to understand the information on the internal electric characteristics of PSCs related to the interface and recombination, we conducted impedance spectroscopy (IS) measurements for the PSCs before and after thermal aging. Fig. 7a and b show the complex impedance plots of the PSCs with t- and

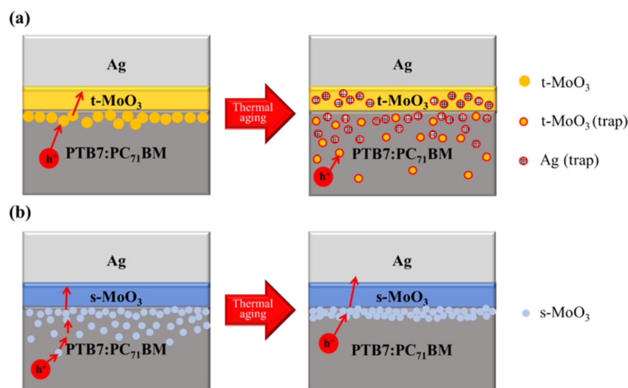

Fig. 6 Schematic representation of (a) thermal diffusion in a device featuring t-MoO_3/Ag as the top electrode and (b) thermal back-diffusion in a device featuring s-MoO_3/Ag as the top electrode.

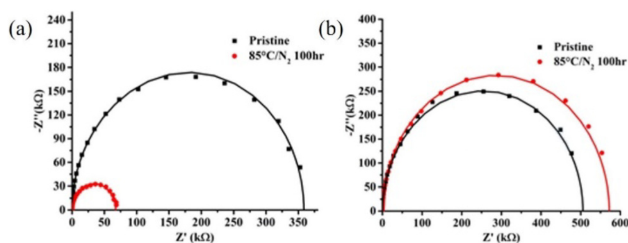

Fig. 7 Complex impedance plots of the (a) t-MoO_3- and (b) s-MoO_3-based PTB7:$PC_{71}BM$/8 PSCs before and after annealing at 85 °C for 100 h (solid lines are fitting curves).

s-MoO_3 HTLs, respectively. The corresponding imaginary component (−Z″)-frequency plots are shown in Fig. S7 (ESI).† The radius of the semicircle in Fig. 7a drastically decreases with the t-MoO_3-based device after thermal aging at 85 °C/N_2 for 100 h, which is consistent with our previous study.[18] The corresponding peak of the imaginary component slightly shifts to high frequency. Both the radius change and peak shift indicate that the geometric capacitance is changed. However, the radius of the semicircle in Fig. 7b slightly increases for the s-MoO_3-based device after thermal aging at 85 °C. The corresponding peak of the imaginary component almost not changes, indicating almost no change in geometric capacitance after thermal aging. The IS measurements show different results in the PSCs based on the t- and s-MoO_3 HTLs. According to IS study,[51] an equivalent circuit mode (Fig. S8†) can be used to fit well the measured IS data as shown in Fig. 7a and b. The fitting result of the model parameters, series resistance (R_s), bulk resistance (R_b), geometric capacitance (C_g), chemical capacitance (C_μ), recombination capacitance (R_{rec}) and average carrier lifetime (τ_{avg}) are listed in Table S3 (ESI).† The key parameter is the average carrier lifetime ($\tau_{avg} = (R_{rec} \times C_\mu)^{1/n}$), where n ranges from 0.95–0.98 in this study. The reduction in the τ_{avg} value leads to the increase in the charge recombination and thus the reduction in PCE, also indicating the increase in the charge traps. The fitted τ_{avg} values of the t-MoO_3-based device before and after thermal aging are 2.89 ms and 0.74 ms, respectively, indicating the large increase in the recombination due to charge traps after aging and thus the reduction in the PCE (*i.e.*, the thermal burn-in loss and the diffusion-in effects of Mo as the traps). On the other hand, the increase in the geometric capacitance C_g consistently shows the increase in charge recombination due to traps for the t-MoO_3-based device. In contrast, the fitted τ_{avg} values of the s-MoO_3-based device before and after thermal aging are almost the same (0.73 ms and 0.68 ms, respectively), indicating no change in charge recombination and PCE (the existence of very few traps and the backward diffusion of MoO_3 from the active layer to HTL).

For evaluating the hole mobility transporting through the HTL and its interface near the active layer (closely related to charge extraction and recombination within HTL), we used the space-charge limited current (SCLC) model to measure the hole mobility of the devices before and after thermal aging at

This journal is © The Royal Society of Chemistry 2023

Published on 03 January 2023. Downloaded by CHANG GUNG UNIVERSITY on 2/9/2023 4:28:16 AM.

85 °C in nitrogen for 100 hours. The hole-only devices have the structure of ITO/PEDOT: PSS/PTB7:$PC_{71}BM$/t-MoO_3 or s-MoO_3/Ag.[52] The corresponding current density–voltage curves are shown in Fig. S9.† The calculated hole mobility of the device based on s-MoO_3 is slightly higher than that of the device based on t-MoO_3 before thermal aging. The calculated hole mobility is comparable to the value reported by the other literature.[52–54] The hole mobility values of both devices with t-MoO_3 and s-MoO_3 show negligible change before and after 100 h of thermal aging, implying that the diffusion of t-MoO_3 and backward diffusion of s-MoO_3 have no influence on hole transport at the interface or within HTL due to their well-dispersity due to small molecule size. The recombination by the charge traps within the active layer is the main factor of degradation.

Stability under damp-heat and light-soaking accelerated tests

We improved the intrinsic thermal stability of PSCs by developing the s-MoO_3 HTL. We were interested in examining whether the stability of the s-MoO_3 HTL could be maintained under damp-heat conditions. We appropriately encapsulated an inverted PSC device featuring s-MoO_3 HTLs and tested them under two damp-heat conditions: (i) 65 °C and 65% RH and (ii) 85 °C and ambient air (*ca.* 45% RH). Fig. 8 presents the evolution of the PCEs of the devices with respect to aging time under the two accelerated-lifetime test conditions. The encapsulated device aged at 85 °C under the ambient air environment had a burn-in loss of approximately 10% and then retained 90% of its initial efficiency after 4400 h. Under the environment at 65 °C and 65% RH, the encapsulated device retained 80% of its initial efficiency after 1350 h. Thus, we suspect that the degradation can be attributed to H_2O and O_2 penetrating through the lateral encapsulation epoxy between the top glass and substrate glass.[55] The invasive H_2O and O_2 accumulated around the PSC device and then caused damage to the top electrode and HTL. This degradation, caused by the extrinsic invasion, would presumably have been inhibited effectively through more effective encapsulation.

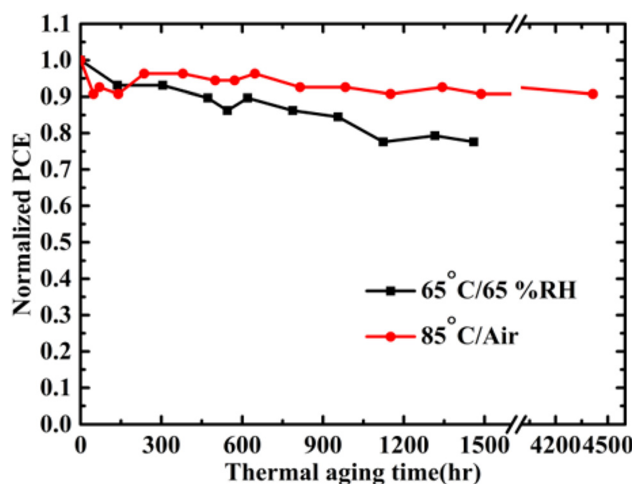

Fig. 8 Variations in the PCEs of encapsulated PTB7:$PC_{71}BM$ devices featuring the s-MoO_3 HTL, plotted with respect to the aging time and measured under damp-heat conditions of 85 °C per ambient air (*ca.* 45% RH) and 65 °C/65% RH.

Light-induced degradation, whose formation mechanisms are complex and still poorly understood, is one of the critical factors affecting the commercialization of OPVs. According to several reviews,[6,56,57] the main mechanisms of light-induced degradation involve photooxidation or chemical degradation of the donors and acceptors in the active layer, including the formation of persistent radical cations on the polymer chains, the photooligomerization of fullerene acceptors, and the photolysis of polymer donors. Such photooxidation reactions can also occur in ZnO ETLs.[58] Recent studies[59] have noted that light impinging upon a thermally deposited MoO_3 HTL (*i.e.*, t-MoO_3 HTL) could result in the formation of Mo^{5+} species. The decrease in the oxidation state in the t-MoO_3 HTL would decrease the work function and lead to large losses in the values of V_{oc} and J_{sc} of the device, thereby decreasing its long-term stability. A similar study[60] found that the Mo^{5+} species were formed at the interface between the P3HT polymer and the thermally deposited MoO_3 HTL ("interfacial photoreduction"), leading to rapid decreases in the values of V_{oc} and the FF of a P3HT: $PC_{61}BM$ PSC during illumination with light. These factors motivated us to investigate whether the devices containing s-MoO_3 HTLs might degrade during light-soaking tests. Fig. S10† presents the degradation curves of the photovoltaic parameters for encapsulated inverted PTB7: $PC_{71}BM$ and P3HT:$PC_{61}BM$ devices incorporating s-MoO_3 HTLs, plotted with respect to time under continuous AM 1.5G solar illumination. The evolution of the PCEs of both devices revealed similar photoinduced burn-in losses (20–23% of the initial values) after 100 h. Both devices also displayed good long-term stability during the period of illumination from 100 to 1200 h. The PCEs of the P3HT: $PC_{61}BM$ and PTB7:$PC_{71}BM$ devices gradually decayed to 75 and 60% of their initial values, respectively, when the period of illumination was extended above 1500 h. A review article[6] indicated that the photoinduced burn-in loss can be attributed to the photooxidation reactions of the polymers and fullerenes in the active layer, mainly decreasing the values of J_{sc} and V_{oc}. Our devices incorporating the s-MoO_3 HTL also displayed superior long-term photostability when compared with those of other studies.[61] We suspect that the degree of photoinduced degradation caused by the s-MoO_3 HTL was much lower than that contributed by photooxidation of the active layer. Nevertheless, our data cannot provide an obvious sign of the photoinduced degradation induced by the s-MoO_3 HTL. New experiments for such an in-depth and independent study will be conducted in the future.

Conclusions

We have demonstrated that inverted PTB7:$PC_{71}BM$ PSCs containing solution-processed s-MoO_3 HTLs that had been subjected to thermal aging at 85 °C in the dark under N_2 can

Published on 03 January 2023. Downloaded by CHANG GUNG UNIVERSITY on 2/9/2023 4:28:16 AM.

retain their initial PCEs, or even slightly increase them, for over 2200 h. In contrast, the PCEs of inverted PSCs featuring thermally deposited MoO_3 HTLs decreased to 80% of their initial values within 200 h, due to burn-in loss; the subsequent long-term stability occurred with a gradual decay to 60% of the initial efficiency over a period of 800 h. The value of T_{80} (or the excellent thermal stability) resulting from the use of this novel s-MoO_3 HTL was up to ten times greater than the currently reported lifetimes for PTB7- and LBG-polymer:PCBM PSCs operated under various heat-equivalent testing conditions. A systematic XPS study of devices featuring both types of HTLs revealed the mechanism responsible for forming the robust HTL and fully preventing thermal degradation. The solution-processed MoO_3 particles in the active layer could, during thermal aging, undergo back-diffusion into the HTL to form a robust layer structure and a sharp interface, thereby fully inhibiting the penetration of Ag atoms from the electrode and from the MoO_3 HTL into the active layer. The value of T_{80} measured under damp-heat conditions of 65 °C/65% RH and the value of T_{90} for 85 °C/air were 1350 and 4400 h, respectively. Here, we attribute the extrinsic degradation to H_2O and O_2 penetrating through the lateral encapsulation epoxy between the top glass and the substrate glass; this problem could presumably be solved through improved encapsulation. The device incorporating the s-MoO_3 HTL also displayed excellent photostability under continuous illumination with AM 1.5G light, relative to that of the recently published counterparts. Thus, the solution-processed MoO_3 HTLs described herein have great potential for replacing commonly used t-MoO_3 HTLs, while also being inexpensive and amenable for low-energy fabrication processes compatible with mass production.

Author contributions

Y. M. S., C. S. T. and Y. C. H. conceived the concept of this study. Y. M. S., H. K. L., H. C. C., T. C. L., and K. W. C. prepared the sample and analyzed the photovoltaic characteristics and stability. C. H. T. C., P. C. J. and J. S. T. performed the XPS characterization. Y. M. S. and C. H. T. C. analyzed the data. C. S. T., Y. C. H., and J. S. T. wrote the manuscript with contributions from all authors.

Conflicts of interest

There are no conflicts to declare.

Acknowledgements

This study was supported financially by the Ministry of Science and Technology of Taiwan (MOST 107-2218-E-131-007-MY3; MOST 109-2112-M-003-013; MOST 110-2112-M-003-018; MOST 110-2221-E-131-010; and MOST 111-2221-E-131-022) and Academia Sinica (AS-SS-109-05).

References

1 Q. Liu, Y. Jiang, K. Jin, J. Qin, J. Xu, W. Li, J. Xiong, J. Liu, Z. Xiao, K. Sun, S. Yang, X. Zhang and L. Ding, *Sci. Bull.*, 2020, **65**, 272–275.
2 S. K. Hau, H.-L. Yip, N. S. Baek, J. Zou, K. O'Malley and A. K. Y. Jen, *Appl. Phys. Lett.*, 2008, **92**, 253301.
3 M. J. Tan, S. Zhong, J. Li, Z. Chen and W. Chen, *ACS Appl. Mater. Interfaces*, 2013, **5**, 4696–4701.
4 X. Hu, L. Chen and Y. Chen, *J. Phys. Chem. C*, 2014, **118**, 9930–9938.
5 J. You, C.-C. Chen, L. Dou, S. Murase, H.-S. Duan, S. A. Hawks, T. Xu, H. J. Son, L. Yu, G. Li and Y. Yang, *Adv. Mater.*, 2012, **24**, 5267–5272.
6 W. R. Mateker and M. D. McGehee, *Adv. Mater.*, 2017, **29**, 1603940.
7 T. Heumueller, W. R. Mateker, I. T. Sachs-Quintana, K. Vandewal, J. A. Bartelt, T. M. Burke, T. Ameri, C. J. Brabec and M. D. McGehee, *Energy Environ. Sci.*, 2014, **7**, 2974–2980.
8 H. Lee, J. Sohn, P. Tyagi and C. Lee, *Appl. Phys. Lett.*, 2017, **110**, 053301.
9 W. Ma, C. Yang, X. Gong, K. Lee and A. J. Heeger, *Adv. Funct. Mater.*, 2005, **15**, 1617–1622.
10 H. C. Wong, Z. Li, C. H. Tan, H. Zhong, Z. Huang, H. Bronstein, I. McCulloch, J. T. Cabral and J. R. Durrant, *ACS Nano*, 2014, **8**, 1297–1308.
11 C.-Y. Chen, C.-S. Tsao, Y.-C. Huang, H.-W. Liu, W.-Y. Chiu, C.-M. Chuang, U. S. Jeng, C.-J. Su, W.-R. Wu, W.-F. Su and L. Wang, *Nanoscale*, 2013, **5**, 7629–7638.
12 H.-C. Liao, C.-S. Tsao, T.-H. Lin, C.-M. Chuang, C.-Y. Chen, U. S. Jeng, C.-H. Su, Y.-F. Chen and W.-F. Su, *J. Am. Chem. Soc.*, 2011, **133**, 13064–13073.
13 Y. Ning, L. Lv, Y. Lu, C. Zhang, Y. Fang, A. Tang, Y. Hu, Z. Lou, F. Teng and Y. Hou, *Phys. Status Solidi RRL*, 2015, **9**, 120–124.
14 J. Bhattacharya, P. H. Joshi, R. Biswas and V. L. Dalal, *Sol. Energy Mater. Sol. Cells*, 2017, **164**, 70–79.
15 N. Li, J. D. Perea, T. Kassar, M. Richter, T. Heumueller, G. J. Matt, Y. Hou, N. S. Güldal, H. Chen, S. Chen, S. Langner, M. Berlinghof, T. Unruh and C. J. Brabec, *Nat. Commun.*, 2017, **8**, 14541.
16 I. T. Sachs-Quintana, T. Heumüller, W. R. Mateker, D. E. Orozco, R. Cheacharoen, S. Sweetnam, C. J. Brabec and M. D. McGehee, *Adv. Funct. Mater.*, 2014, **24**, 3978–3985.
17 Y.-J. Hsieh, Y.-C. Huang, W.-S. Liu, Y.-A. Su, C.-S. Tsao, S.-P. Rwei and L. Wang, *ACS Appl. Mater. Interfaces*, 2017, **9**, 14808–14816.
18 Y. M. Sung, Y. C. Huang, F. S. S. Chien and C. S. Tsao, *IEEE J. Photovolt.*, 2019, **9**, 694–699.
19 W. Greenbank, L. Hirsch, G. Wantz and S. Chambon, *Appl. Phys. Lett.*, 2015, **107**, 263301.
20 F. Hermerschmidt, A. Savva, E. Georgiou, S. M. Tuladhar, J. R. Durrant, I. McCulloch, D. D. C. Bradley, C. J. Brabec, J. Nelson and S. A. Choulis, *ACS Appl. Mater. Interfaces*, 2017, **9**, 14136–14144.

This journal is © The Royal Society of Chemistry 2023

Published on 03 January 2023. Downloaded by CHANG GUNG UNIVERSITY on 2/9/2023 4:28:16 AM.

21 W. Greenbank, N. Rolston, E. Destouesse, G. Wantz, L. Hirsch, R. Dauskardt and S. Chambon, *J. Mater. Chem. A*, 2017, **5**, 2911–2919.
22 J. Griffin, D. C. Watters, H. Yi, A. Iraqi, D. Lidzey and A. R. Buckley, *Adv. Energy Mater.*, 2013, **3**, 903–908.
23 M. Ahmadpour, A. L. F. Cauduro, C. Méthivier, B. Kunert, C. Labanti, R. Resel, V. Turkovic, H.-G. Rubahn, N. Witkowski, A. K. Schmid and M. Madsen, *ACS Appl. Energy Mater.*, 2019, **2**, 420–427.
24 M. C. Gwinner, R. D. Pietro, Y. Vaynzof, K. J. Greenberg, P. K. H. Ho, R. H. Friend and H. Sirringhaus, *Adv. Funct. Mater.*, 2011, **21**, 1432–1441.
25 N. K. Elumalai, A. Saha, C. Vijila, R. Jose, Z. Jie and S. Ramakrishna, *Phys. Chem. Chem. Phys.*, 2013, **15**, 6831–6841.
26 K. Zilberberg, H. Gharbi, A. Behrendt, S. Trost and T. Riedl, *ACS Appl. Mater. Interfaces*, 2012, **4**, 1164–1168.
27 W. Qiu, R. Müller, E. Voroshazi, B. Conings, R. Carleer, H.-G. Boyen, M. Turbiez, L. Froyen, P. Heremans and A. Hadipour, *ACS Appl. Mater. Interfaces*, 2015, **7**, 3581–3589.
28 J.-H. Kim, E.-K. Park, J.-H. Kim, H. J. Cho, D.-H. Lee and Y.-S. Kim, *Electron. Mater. Lett.*, 2016, **12**, 383–387.
29 Y. Wang, Q. Luo, N. Wu, Q. Wang, H. Zhu, L. Chen, Y.-Q. Li, L. Luo and C.-Q. Ma, *ACS Appl. Mater. Interfaces*, 2015, **7**, 7170–7179.
30 M. O. Reese, S. A. Gevorgyan, M. Jørgensen, E. Bundgaard, S. R. Kurtz, D. S. Ginley, D. C. Olson, M. T. Lloyd, P. Morvillo, E. A. Katz, A. Elschner, O. Haillant, T. R. Currier, V. Shrotriya, M. Hermenau, M. Riede, K. R. Kirov, G. Trimmel, T. Rath, O. Inganäs, F. Zhang, M. Andersson, K. Tvingstedt, M. Lira-Cantu, D. Laird, C. McGuiness, S. Gowrisanker, M. Pannone, M. Xiao, J. Hauch, R. Steim, D. M. DeLongchamp, R. Rösch, H. Hoppe, N. Espinosa, A. Urbina, G. Yaman-Uzunoglu, J.-B. Bonekamp, A. J. J. M. van Breemen, C. Girotto, E. Voroshazi and F. C. Krebs, *Sol. Energy Mater. Sol. Cells*, 2011, **95**, 1253–1267.
31 M. Nam, M. Cha, H. H. Lee, K. Hur, K. T. Lee, J. Yoo, I. K. Han, S. J. Kwon and D. H. Ko, *Nat. Commun.*, 2017, **8**, 14068.
32 H. Wang, C. Xie, W. Zhang, S. Cai, Z. Yang and Y. Gui, *J. Hazard. Mater.*, 2007, **141**, 645–652.
33 S. Ayyappan and C. N. R. Rao, *Mater. Res. Bull.*, 1995, **30**, 947–951.
34 F. Xie, W. C. H. Choy, C. Wang, X. Li, S. Zhang and J. Hou, *Adv. Mater.*, 2013, **25**, 2051–2055.
35 https://store-us.semi.org/products/pv07600-semi-pv76-test-method-for-durability-of-low-light-intensity-organic-photovoltaic-opv-and-dye-sensitized-solar-cell-dssc.
36 C.-P. Chen, Y.-Y. Tsai, Y.-C. Chen and Y.-H. Li, *Sol. Energy*, 2018, **176**, 170–177.
37 M. Tessarolo, A. Guerrero, D. Gedefaw, M. Bolognesi, M. Prosa, X. Xu, M. Mansour, E. Wang, M. Seri, M. R. Andersson, M. Muccini and G. Garcia-Belmonte, *Sol. Energy Mater. Sol. Cells*, 2015, **141**, 240–247.
38 S. Chambon, L. Derue, M. Lahaye, B. Pavageau, L. Hirsch and G. Wantz, *Materials*, 2012, **5**, 2521–2536.
39 Z. Zhang, Y. Xiao, H.-X. Wei, G.-F. Ma, S. Duhm, Y.-Q. Li and J.-X. Tang, *Appl. Phys. Express*, 2013, **6**, 095701.
40 R. Rösch, D. M. Tanenbaum, M. Jørgensen, M. Seeland, M. Bärenklau, M. Hermenau, E. Voroshazi, M. T. Lloyd, Y. Galagan, B. Zimmermann, U. Würfel, M. Hösel, H. F. Dam, S. A. Gevorgyan, S. Kudret, W. Maes, L. Lutsen, D. Vanderzande, R. Andriessen, G. Teran-Escobar, M. Lira-Cantu, A. Rivaton, G. Y. Uzunoğlu, D. Germack, B. Andreasen, M. V. Madsen, K. Norrman, H. Hoppe and F. C. Krebs, *Energy Environ. Sci.*, 2012, **5**, 6521–6540.
41 P. Romero-Gomez, R. Betancur, A. Martinez-Otero, X. Elias, M. Mariano, B. Romero, B. Arredondo, R. Vergaz and J. Martorell, *Sol. Energy Mater. Sol. Cells*, 2015, **137**, 44–49.
42 Irfan, H. Ding, Y. Gao, C. Small, D. Y. Kim, J. Subbiah and F. So, *Appl. Phys. Lett.*, 2010, **96**, 243307.
43 S. Guo, B. Cao, W. Wang, J.-F. Moulin and P. Müller-Buschbaum, *ACS Appl. Mater. Interfaces*, 2015, **7**, 4641–4649.
44 J. Chen, J. Cao, L. Liu, L. Xie, H. Zhou, J. Zhang, K. Zhang, M. Xiao and F. Huang, *Adv. Funct. Mater.*, 2022, **32**, 2200629.
45 M. H. Elsayed, B.-H. Jiang, Y.-P. Wang, P.-Y. Chang, Y.-C. Chiu, R.-J. Jeng, H.-H. Chou and C.-P. Chen, *J. Mater. Chem. A*, 2021, **9**, 9780–9790.
46 Y. Han, H. Dong, W. Pan, B. Liu, X. Chen, R. Huang, Z. Li, F. Li, Q. Luo, J. Zhang, Z. Wei and C.-Q. Ma, *ACS Appl. Mater. Interfaces*, 2021, **13**, 17869–17881.
47 Y. Wang, J. Han, L. Cai, N. Li and Z. Li, *J. Mater. Chem. A*, 2020, **8**, 21255–21264.
48 W. Lan, J. Gu, X. Gao, C. Gong, Y. Liu, W. Zhang, Y. Sun, T. Yue, B. Wei and F. Zhu, *Adv. Mater. Interfaces*, 2022, 2101894.
49 W. Lan, J. Gu, S. Wu, Y. Peng, M. Zhao, Y. Liao, T. Xu, B. Wei, L. Ding and F. Zhu, *EcoMat*, 2021, 1–10.
50 T. Goh, J.-S. Huang, B. Bartolome, M. Y. Sfeir, M. Vaisman, M. L. Lee and A. D. Taylor, *J. Mater. Chem. A*, 2015, **3**, 18611–18621.
51 B. J. Leever, C. A. Bailey, T. J. Marks, M. C. Hersam and M. F. Durstock, *Adv. Energy Mater.*, 2012, **2**, 120–128.
52 J. Xiao, Z. Chen, G. Zhang, Q.-Y. Li, Q. Yin, X.-F. Jiang, F. Huang, Y.-X. Xu, H.-L. Yip and Y. Cao, *J. Mater. Chem. C*, 2018, **6**, 4457.
53 B. Ebenhoch, S. A. J. Thomson, K. Genevičius, G. Juška and I. D. W. Samuel, *Org. Electron.*, 2015, **22**, 62.
54 S. Foster, F. Deledalle, A. Mitani, T. Kimura, K.-B. Kim, T. Okachi, T. Kirchartz, J. Oguma, K. Miyake, J. R. Durrant, S. Doi and J. Nelson, *Adv. Energy Mater.*, 2014, 1400311.
55 C.-Y. Lee, C.-S. Tsao, H.-K. Lin, H.-C. Cha, T.-Y. Chung, Y.-M. Sung and Y.-C. Huang, *Sol. Energy*, 2021, **213**, 136–144.
56 P. Cheng and X. Zhan, *Chem. Soc. Rev.*, 2016, **45**, 2544–2582.

57 M. Jørgensen, K. Norrman, S. A. Gevorgyan, T. Tromholt, B. Andreasen and F. C. Krebs, *Adv. Mater.*, 2012, **24**, 580–612.
58 A. Manor, E. A. Katz, T. Tromholt and F. C. Krebs, *Adv. Energy Mater.*, 2011, **1**, 836–843.
59 H. Zhang, A. Borgschulte, F. A. Castro, R. Crockett, A. C. Gerecke, O. Deniz, J. Heier, S. Jenatsch, F. Nüesch, C. Sanchez-Sanchez, A. Zoladek-Lemanczyk and R. Hany, *Adv. Energy Mater.*, 2015, **5**, 1400734.
60 H. Gu, L. Yan, S. Saxena, X. Shi, X. Zhang, Z. Li, Q. Luo, H. Zhou, Y. Yang, X. Liu, W. W. H. Wong and C.-Q. Ma, *ACS Appl. Energy Mater.*, 2020, **3**, 9714–9723.
61 F. J. Lim, A. Krishnamoorthy and G. W. Ho, *ACS Appl. Mater. Interfaces*, 2015, **7**, 12119–12127.

Published on 03 January 2023. Downloaded by CHANG GUNG UNIVERSITY on 2/9/2023 4:28:16 AM.